HOKKAIDO UNIVERSITY

Title	Reconstruction of the Eddy Current Distribution on the Vacuum Vessel in a Reversed Field Pinch Device based on the External Magnetic Sensor Signals
Author(s)	ITAGAKI, Masafumi; SANPEI, Akio; MASAMUNE, Sadao et al.
Citation	Plasma and Fusion Research, 9, 1402046 https://doi.org/10.1585/pfr.9.1402046
Issue Date	2014-05-07
Doc URL	https://hdl.handle.net/2115/58439
Type	journal article
File Information	r2014_09-1402046.pdf

Hokkaido University Collection of Scholarly and Academic Papers : HUSCAP

Reconstruction of the Eddy Current Distribution on the Vacuum Vessel in a Reversed Field Pinch Device based on the External Magnetic Sensor Signals

Masafumi ITAGAKI, Akio SANPEI[1)], Sadao MASAMUNE[1)] and Kiyomasa WATANABE[2)]

Faculty of Engineering, Hokkaido University, Sapporo, Hokkaido 060-8628, Japan
[1)]*Graduate School of Science and Technology, Kyoto Institute of Technology, Kyoto 606-8585, Japan*
[2)]*National Institute for Fusion Science, Toki, Gifu 509-5292, Japan*

(Received 30 November 2013 / Accepted 17 March 2014)

For the MHD equilibrium reconstruction of a reverse field pinch device, it is a big issue to identify accurately the strong eddy current flow on the shell. In the present work, boundary integrals of the eddy current along the shell are added to the conventional Cauchy-condition surface method formulation. The eddy current profile is unknown in advance but straightforwardly identified using only the signals from magnetic sensors located outside the plasma. Two ideas are introduced to overcome the numerical difficulties encountered in the problem. One is an accurate boundary integral scheme to damp out the near singularity occurring at the sensor position very close to the shell. The other is the modified truncated singular value decomposition technique to solve an ill-conditioned matrix equation when a large number of nodal points exist on the shell. The capability of the new method is demonstrated for a test problem modeling the RELAX device.

© *2014 The Japan Society of Plasma Science and Nuclear Fusion Research*

Keywords: reversed field pinch, RELAX, eddy current, Cauchy condition surface method, singular boundary integral, modified truncated SVD method

DOI: 10.1585/pfr.9.1402046

1. Introduction

The identification of the MHD equilibrium configuration is important for the energy confinement and the stability of fusion plasma from both operating control and analytical points of view. To identify the equilibrium configuration, the magnetic field or flux profile outside the plasma and hence the plasma boundary shape are highly important. Such information should be deduced from signals of magnetic sensors located outside the plasma, since the direct measurement of physical quantities inside the plasma is usually difficult.

The Cauchy condition surface (CCS) method [1, 2] is one such idea for reconstructing the magnetic flux distributions around the boundary of the plasma, whose MHD configuration is originally assumed to be axisymmetric in the toroidal direction. The method has already been established for operating control and diagnosis of JT-60U, a tokamak-type device. Furthermore, Itagaki *et al.* recently developed the 3D CCS method [3–5] to reconstruct the 3D magnetic field profile outside the non-axisymmetric plasma in the Large Helical Device (LHD). In these methods, the CCS, where both the Dirichlet and the Neumann conditions are unknown, is hypothetically placed in a domain that can be supposed to be inside the plasma. The CCS plays the same role as the plasma current in causing the field outside the plasma.

In all the above analyses, however, the eddy current generated on the vacuum vessel was neglected. In a reverse field pinch (RFP) device such as the RELAX [6] at Kyoto Institute of Technology, a strong eddy current is generated on the shell (vacuum vessel) wall, which is closely related to local MHD equilibrium. For example, the eddy current flow is modified at port holes to produce localized field errors which have strong influence on the edge magnetic structure and edge transport, because the toroidal field is rather weak in comparison with the poloidal field at the edge in the RFP configuration.

Even in tokamaks the behavior of the eddy current in case of a plasma disruption is important from the viewpoint of the plasma position and shape control. The eddy current also plays an important part in the so-called RWM (resistive wall mode) event [7–9]. The electric circuit model has been often adopted for an estimation of the eddy current profile, but it is not a straightforward way based upon only a magnetic measurement. In these situations, one possible idea is that the eddy current effect is incorporated into the original CCS method algorithm for a reliable reconstruction of magnetic field/flux structure. However, the number of such eddy current adjusted reconstruction analyses is very limited. In the idea by Kurihara *et al.* for the JT-60U [10], the eddy current effect is considered as a forward problem. That is, the vacuum vessel is simulated by multiple one-turn filament coils, and then the

author's e-mail: itagaki@qe.eng.hokudai.ac.jp

© 2014 The Japan Society of Plasma Science and Nuclear Fusion Research

eddy current results are taken into the inverse analysis using a CCS method code. Nakamura *et al.* proposed an improved CCS technique [11] to identify the plasma shape in the spherical tokamak QUEST at Kyushu University. In their method the vacuum vessel is divided into 8 parts, in each of which filaments are assumed to represent the eddy currents, so that these eddy current contributions are added to each boundary integral equation as a new term in the CCS method formulation.

In the present paper the authors propose a more advanced CCS method where the eddy current term is given by a boundary integral along the shell in the poloidal direction. It should be noticed here that the eddy current profile on the shell is not given in advance but completely unknown before one starts the analysis. The main purpose of this work is to identify the eddy current profile straightforwardly using only the signals from magnetic sensors located outside the plasma. That is, one solves the Cauchy conditions and the eddy current profile simultaneously. Kurihara *et al.* reported in Ref. [10] that they had faced an ill-posed problem in their attempt similar to the authors' work. In the present work the authors introduce two ideas to overcome this difficulty. One is an accurate boundary integral scheme to damp out the near singularity occurring at the sensor position very close to the shell. The other is the modified truncated singular value decomposition (MTSVD) technique to solve an ill-conditioned matrix equation when a large number of nodal points exist on the shell. The capability of the new method is demonstrated for a test problem modeling the RELAX device.

This paper is arranged as follows. Section 2.1 reviews the original CCS method previously reported in Ref. [1]. Section 2.2 describes how the boundary integral of the eddy current density is newly incorporated into the CCS method formulation. The set of boundary integral equations is converted to a matrix equation form as described in Sec. 2.3. An algorithm is introduced in Sec. 2.4 to eliminate the singularity in the boundary integral along the shell, which is caused by the sensor locations very close to the shell. The MTSVD technique is introduced in Sec. 2.5 to solve an ill-conditioned matrix equation.

A numerical demonstration for the RELAX device is given in Sec. 3. Sections 3.2 and 3.3 describe the reconstruction results of the eddy current density profile and the magnetic flux profile, respectively. Section 3.4 reports the influence of the sensor signal noise to the reconstructed solutions.

2. Method

The Cauchy-condition surface (CCS) method [1] is an inverse analytic technique to identify the plasma boundary shape. In this section, one describes how the effect of the eddy current on the shell is incorporated into the original CCS method. It should be noted that in the present work the eddy current distribution on the shell, in the same way as all other physical quantities, is assumed to be axisymmetric in the toroidal direction.

2.1 Outline of the original CCS method

The Cauchy-condition surface (CCS), where both the Dirichlet and the Neumann conditions (i.e., the magnetic flux function ψ and its normal derivative $\partial\psi/\partial n$) are unknown, is hypothetically placed in a domain that can be supposed to be inside the plasma. In the analysis, no plasma current is assumed outside this CCS, where in reality plasma current does exist. Instead, the CCS plays the same role as the plasma current in causing the field outside the plasma.

For an axisymmetric (r, z) system, the differential form of Ampere's law $\mu_0 \boldsymbol{j} = \nabla \times \boldsymbol{B}$ can be reduced to a partial differential equation

$$
\begin{aligned}
-\Delta^*\psi \equiv -\left\{ r\frac{\partial}{\partial r}\left(\frac{1}{r}\frac{\partial}{\partial r}\right) + \frac{\partial^2}{\partial z^2}\right\}\psi \\
= \mu_0 r(j_{\mathrm{Pl}} + j_{\mathrm{Coil}} + j_{\mathrm{Eddy}}),
\end{aligned} \tag{1}
$$

in terms of magnetic flux function ψ. Here, j_{Pl}, j_{Coil}, and j_{Eddy} denote the toroidal components of the plasma current, the external coil current and the eddy current respectively. The quantity μ_0 is the permeability of a vacuum. In the following formulation one uses the magnetic flux $\tilde{\psi} = 2\pi\psi$ [Wb] instead of the magnetic flux function ψ [Wb/rad] because the physical quantity directly measured is the magnetic flux. Also, instead of the magnetic field signal B, a quantity $\tilde{B} = 2\pi B$ is defined.

To evaluate $\tilde{\psi}$ and $\partial\tilde{\psi}/\partial n$ at several points along the CCS (Γ_{CCS}), three types of boundary integral equations (BIEs) for the vacuum field can be given using the sensor signals and the external poloidal coil current data, as shown below.

(i) For the magnetic 'flux' signal $\tilde{\psi}_i$ located at points i:

$$
\tilde{\psi}_i - \tilde{W}_i^{\psi} = \int_{\Gamma_{\mathrm{CCS}}} \left(\frac{\psi^*}{r}\frac{\partial\tilde{\psi}}{\partial n} - \frac{\tilde{\psi}}{r}\frac{\partial\psi^*}{\partial n} \right) \mathrm{d}\Gamma. \tag{2a}
$$

(ii) For the magnetic 'field' signal B_i located at points i:

$$
\tilde{B}_i - \tilde{W}_i^{B} = \int_{\Gamma_{\mathrm{CCS}}} \left(\frac{B^*}{r}\frac{\partial\tilde{\psi}}{\partial n} - \frac{\tilde{\psi}}{r}\frac{\partial B^*}{\partial n} \right) \mathrm{d}\Gamma, \tag{2b}
$$

using the quantity $\tilde{B}_i = 2\pi B_i$, where $B_i = -\boldsymbol{n}_0 \cdot \nabla\psi_i / r_i$, $B^* = -\boldsymbol{n}_0 \cdot \nabla\psi^*/r$ with $\boldsymbol{n}_0$ being the assigned vector normal to the direction of the 'magnetic probe' located at the point i.

(iii) For points i on the Cauchy condition surface:

$$
\frac{1}{2}\tilde{\psi}_i - \tilde{W}_i^{C} = \int_{\Gamma_{\mathrm{CCS}}} \left(\frac{\psi^*}{r}\frac{\partial\tilde{\psi}}{\partial n} - \frac{\tilde{\psi}}{r}\frac{\partial\psi^*}{\partial n} \right) \mathrm{d}\Gamma. \tag{2c}
$$

In Eqs. (2a)-(2c), $\tilde{W}_i^{\psi}$, $\tilde{W}_i^{B}$ and $\tilde{W}_i^{C}$ are the contributions of the external coil currents to the point i. In each

equation, ψ^* denotes the fundamental solution which satisfies a subsidiary equation

$$-\left\{r\frac{\partial}{\partial r}\left(\frac{1}{r}\frac{\partial}{\partial r}\right)+\frac{\partial^2}{\partial z^2}\right\}\psi^* = r\delta_i, \tag{3}$$

where Dirac's delta function δ_i means $\delta(r-a)\delta(z-b)$ with the spike at the point i, where i is defined as having the coordinates (a,b). Physically Eq. (3) describes the magnetic flux function for an arbitrary field point (r,z) caused by a unit toroidal current located at the point (a,b). The detailed form of ψ^* is given by [1,2]

$$\psi^* = \frac{\sqrt{ar}}{\pi k}\left[\left(1-\frac{k^2}{2}\right)K(k)-E(k)\right], \tag{4}$$

with

$$k^2 = \frac{4ar}{(r+a)^2+(z-b)^2}, \tag{5}$$

where $K(k)$ and $E(k)$ are the complete elliptic integrals of the first and the second kind, respectively. In the original CCS method, Eqs. (2a), (2b) and (2c) are discretized and coupled and can be expressed in a matrix form. Once all the values of $\partial\tilde{\psi}/\partial n$ and $\tilde{\psi}$ along the CCS have been given by solving the matrix equation in a least square sense, the distribution of magnetic flux $\tilde{\psi}_i$ can be calculated using Eq. (2a) for arbitrary points 'i'. Thus, the outermost magnetic flux surface can be found by drawing contours of magnetic flux.

2.2 Incorporation of the eddy current effect into the CCS method formulation

Now one considers the case where the eddy current on the shell cannot be neglected. In this case the BIEs (2a), (2b) and (2c) can be modified as follows.

(i) For the magnetic 'flux' signal $\tilde{\psi}_i$ at points i:

$$\tilde{\psi}_i - \tilde{W}_i^{\psi} = \int_{\Gamma_{\rm CCS}}\left(\frac{\psi^*}{r}\frac{\partial\tilde{\psi}}{\partial n}-\frac{\tilde{\psi}}{r}\frac{\partial\psi^*}{\partial n}\right)\mathrm{d}\Gamma + 2\pi\mu_0\int_{\Gamma_{\rm Shell}} j_S(\boldsymbol{r}_s)\psi^*(\boldsymbol{r}_s\to\boldsymbol{r}_i)\,\mathrm{d}\Gamma(\boldsymbol{r}_s). \tag{6a}$$

(ii) For the magnetic 'field' signal B_i at points i:

$$\tilde{B}_i - \tilde{W}_i^{B} = \int_{\Gamma_{\rm CCS}}\left(\frac{B^*}{r}\frac{\partial\tilde{\psi}}{\partial n}-\frac{\tilde{\psi}}{r}\frac{\partial B^*}{\partial n}\right)\mathrm{d}\Gamma + 2\pi\mu_0\int_{\Gamma_{\rm Shell}} j_S(\boldsymbol{r}_s)B^*(\boldsymbol{r}_s\to\boldsymbol{r}_i)\,\mathrm{d}\Gamma(\boldsymbol{r}_s). \tag{6b}$$

(iii) For points i on the Cauchy condition surface:

$$\frac{1}{2}\tilde{\psi}_i - \tilde{W}_i^{C} = \int_{\Gamma_{\rm CCS}}\left(\frac{\psi^*}{r}\frac{\partial\tilde{\psi}}{\partial n}-\frac{\tilde{\psi}}{r}\frac{\partial\psi^*}{\partial n}\right)\mathrm{d}\Gamma + 2\pi\mu_0\int_{\Gamma_{\rm Shell}} j_S(\boldsymbol{r}_s)\psi^*(\boldsymbol{r}_s\to\boldsymbol{r}_i)\,\mathrm{d}\Gamma(\boldsymbol{r}_s). \tag{6c}$$

The second term on the RHS in each of Eqs. (6a), (6b) and (6c) describes the effect of the eddy current on the shell. The fundamental solution $\psi^*(\boldsymbol{r}_s\to\boldsymbol{r}_i)$ is exactly the same as Eq. (4), but $\boldsymbol{r}_s$ means an arbitrary point on the shell. The quantity $j_S(\boldsymbol{r}_s)$ denotes the linear density [MA/m] distribution of the eddy current on the shell, which is integrated in the poloidal direction along the shell ($\Gamma_{\rm Shell}$).

Only the second integral term on the RHS in each of Eqs. (6a)-(6c) includes the permeability of a vacuum μ_0. With the value of $\mu_0 = 4\pi\times10^{-7}$ [Wb/(A·m)], the numerical integrals along the shell have extremely small values in comparison with the corresponding integrals (not including μ_0) for the CCS. This causes a very large condition number of the resultant matrix and hence inaccurate solution results. To avoid such a problem, the value of μ_0 is set to be 0.4π. This means that the eddy current density results directly given by the computation have a unit of not [A/m] but [MA/m], although it is easily converted into any unit.

2.3 Discretization

One here introduces the quadratic boundary elements [12] for the CCS in such a way that each element has three nodes and hence a total of N_C nodal points are located along the CCS (Note that the number of elements is $N_C/2$). In the same manner, one places N_S eddy current nodes and $N_S/2$ elements on the shell, as illustrated in Fig. 1. That is, the coordinates (r_s, z_s) and the linear eddy current density

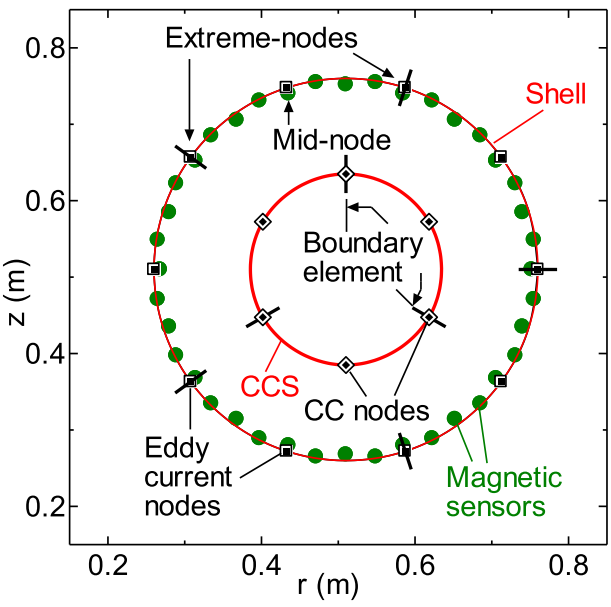

Fig. 1 Quadratic element model for the eddy current distribution on the shell. In this example, 5 elements, i.e., 10 eddy current nodes are placed on the shell.

$j_S(r_s, z_s)$ on the shell are given by

$$r_s = \phi_1 r_1 + \phi_2 r_2 + \phi_3 r_3, \quad z_s = \phi_1 z_1 + \phi_2 z_2 + \phi_3 z_3, \tag{7a}$$

and

$$j_S(r_s, z_s) = \phi_1 j_{S,1} + \phi_2 j_{S,2} + \phi_3 j_{S,3}, \tag{7b}$$

respectively, using the three adjacent coordinates and current density values. Here the interpolation functions are

$$\phi_1 = \xi(\xi - 1)/2, \quad \phi_2 = (1 - \xi)(1 + \xi) \quad \text{and} \quad \phi_3 = \xi(1 + \xi)/2, \tag{8}$$

which are functions of the dimensionless local coordinate ξ ($-1 \le \xi \le 1$).

Let one consider for instance the second integral term on the RHS of Eq. (6a). The integral for the 'j'th element on the shell can be transformed as

$$\mu_0 \int_{\Gamma_{\text{Shell,j}}} j_S \psi^* \mathrm{d}\Gamma = \int_{\Gamma_{\text{Shell,j}}} \mu_0 [\phi_1, \phi_2, \phi_3] \psi^* \mathrm{d}\Gamma \begin{Bmatrix} j_{S,1} \\ j_{S,2} \\ j_{S,3} \end{Bmatrix} = \left[h_1^j, h_2^j, h_3^j\right] \begin{Bmatrix} j_{S,1} \\ j_{S,2} \\ j_{S,3} \end{Bmatrix}, \tag{9}$$

where

$$h_1^j = \int_{\Gamma_{\text{Shell,j}}} \mu_0 \phi_1 \psi^* \mathrm{d}\Gamma, \quad h_2^j = \int_{\Gamma_{\text{Shell,j}}} \mu_0 \phi_2 \psi^* \mathrm{d}\Gamma \quad \text{and} \quad h_3^j = \int_{\Gamma_{\text{Shell,j}}} \mu_0 \phi_3 \psi^* \mathrm{d}\Gamma. \tag{10}$$

The above technique is exactly the same as that adopted for the CCS when the singular point i is not located on a boundary element [13, 14]. For an element on the CCS which includes the singularity, the integration is performed sophisticatedly with the aid of the logarithmic Gaussian quadrature formula [12].

In this way, Eqs. (6a), (6b) and (6c) are discretized, coupled and can be expressed in a matrix form

$$\boldsymbol{D}\boldsymbol{p} = \boldsymbol{g}, \tag{11}$$

where $\boldsymbol{D}$ is an $m \times n$ matrix. Note here that the solution vector $\boldsymbol{p}$ contains N_S nodal points of linear eddy current density (j_S) on the shell as well as the set of N_C flux functions (ψ) and their N_C normal derivatives ($\partial\psi/\partial n$) on the CCS. That is, the total number of unknowns is

$$n = 2N_C + N_S, \tag{12}$$

while the number of BIEs is given by

$$m = N_\psi + N_B + N_C, \tag{13}$$

with N_ψ and N_B being the numbers of flux loops and field sensors, respectively. The quantities, $\psi_i - W_i^\psi$ and $B_i - W_i^B$, where the external coil effects are subtracted from the sensor signals, are stored in the right-hand side vector $\boldsymbol{g}$ in Eq. (11).

The matrix Eq. (11) is solved using the singular value decomposition (SVD) technique [15] in such a way that the least square norm $\|\boldsymbol{D}\boldsymbol{p} - \boldsymbol{g}\|$ is minimized. The $m \times n$ matrix $\boldsymbol{D}$ is decomposed as $\boldsymbol{D} = \boldsymbol{U}\boldsymbol{\Lambda}\boldsymbol{V}^{\mathrm{T}}$, where $\boldsymbol{U}$ and $\boldsymbol{V}^{\mathrm{T}}$ are orthogonal matrices and $\boldsymbol{\Lambda}$ is a diagonal matrix with positive singular values or zero components. The solution in this case is given by

$$\boldsymbol{p} = \boldsymbol{V}\boldsymbol{\Lambda}^{-1}\boldsymbol{U}^{\mathrm{T}}\boldsymbol{g}. \tag{14}$$

As the number of unknowns on the CCS is 12, the total number of unknowns given by Eq. (12) becomes $n = 12 + N_S$.

Once all the values of the Cauchy conditions on the CCS and the linear eddy current densities on the shell nodes are known, the magnetic flux $\tilde{\psi}_i$ for arbitrary points outside the CCS can be calculated using Eq. (6a).

2.4 Accurate computation of boundary integrals along the shell

The boundary integrals along the shell (the second term on the RHS in each of Eqs. (6a), (6b) and (6c)) should be performed very carefully. Since the distance $\varepsilon = \sqrt{(r-a)^2 + (z-b)^2}$ between the sensor position (a, b) and an integration point (r, z) on the shell is very short, the following singularities [14]

$$\psi^* \to -\frac{a}{2\pi} \log \varepsilon, \tag{15}$$

$$\frac{\partial \psi^*}{\partial a} \to -\frac{1}{4\pi} \log \varepsilon + \frac{a(r-a)}{2\pi} \cdot \frac{1}{\varepsilon^2}, \tag{16}$$

and

$$\frac{\partial \psi^*}{\partial b} \to \frac{a(z-b)}{2\pi} \cdot \frac{1}{\varepsilon^2}, \tag{17}$$

arise in the integration kernels when $\varepsilon \to 0$.

The following 'subtraction technique' is often used to eliminate these singularities in a boundary integral [14]. In a boundary element ($\Gamma_{\text{Shell},j}$) along the shell, one here uses the notations $G(\xi)$ and $\phi(\xi)$ for the Jacobian of the coordinate transformation and one of the interpolation functions given by Eq. (8), respectively. Suppose that $B^*(\xi)$ is the fundamental solution or its derivative, while $F_S(\xi)$ denotes the corresponding asymptotic function, i.e., Eqs. (15), (16) or (17). In this case the general form of the boundary integral over $\Gamma_{\text{Shell},j}$ can be rearranged as

$$\begin{aligned} &\int_{-1}^{1} \phi(\xi) G(\xi) B^*(\xi)\, \mathrm{d}\xi \\ &= \int_{-1}^{1} \{\phi(\xi) G(\xi) B^*(\xi) - \phi_0 G_0 F_S(\xi)\} \mathrm{d}\xi \\ &\quad + \phi_0 G_0 \int_{-1}^{1} F_S(\xi)\, \mathrm{d}\xi, \end{aligned} \tag{18}$$

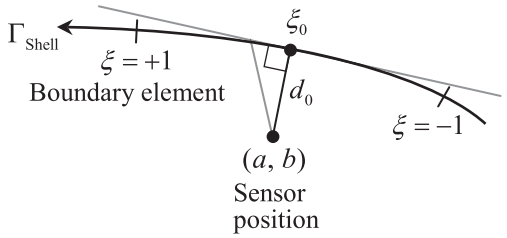

Fig. 2 The minimum distance d_0 from the sensor position (a, b) to a boundary element.

where G_0 and ϕ_0 are the values of $G(\xi)$ and $\phi(\xi)$ at the position $\xi = \xi_0$ on the boundary element that is the nearest to the location of the magnetic sensor i under consideration. The asymptotic function is subtracted from the original integrand in the first integral on the RHS of Eq. (18), and this subtraction is compensated by the analytical integral of the second integral on the RHS. The total integrand of the first integral has no singularity and can therefore be evaluated with the ordinary Gaussian quadrature [12] with 16 integration points for each boundary element.

Ma and Kamiya [16] proposed the use of an approximated 'distance function' for the boundary element adjacent to the sensor position (a, b) as

$$d(\xi) = G_0 \sqrt{(\xi - \xi_0)^2 + (d_0/G_0)^2}, \tag{19}$$

where d_0 is the minimum distance from the point (a, b) to the boundary element as shown in Fig. 2, which corresponds to the local coordinate $\xi = \xi_0$. This distance function agrees with ε in Eqs. (15), (16) and (17) when $\xi \to \xi_0$ and $d_0 \to 0$.

If one defines the (r, z) coordinates corresponding to $\xi = -1$, 0 and 1 on the quadratic boundary element as (r_1, z_1), (r_2, z_2) and (r_3, z_3), the coordinate at an arbitrary point on the element can be given by

$$(r, z) = (p_2\xi^2 + p_1\xi + r_2, q_2\xi^2 + q_1\xi + z_2), \tag{20}$$

with constants p_1, p_2, q_1 and q_2. Then the quantity in Eq. (16) is rewritten using constants α_0, α_1 and α_2, as,

$$\begin{aligned}\frac{a(r-a)}{2\pi}\cdot\frac{1}{\varepsilon^2} &= \frac{a}{2\pi}\cdot\frac{p_2\xi^2 + p_1\xi + r_2 - a}{G_0^2\{(\xi-\xi_0)^2 + (d_0/G_0)^2\}} \\ &= \frac{a}{2\pi G_0^2}\cdot\left[\alpha_0 + \frac{\alpha_1(\xi-\xi_0)}{(\xi-\xi_0)^2 + (d_0/G_0)^2} \right. \\ &\quad \left. + \frac{\alpha_2}{(\xi-\xi_0)^2 + (d_0/G_0)^2}\right].\end{aligned} \tag{21}$$

Similarly, the quantity in Eq. (17) is rewritten as,

$$\begin{aligned}\frac{a(z-b)}{2\pi}\cdot\frac{1}{\varepsilon^2} &= \frac{a}{2\pi G_0^2}\cdot\left[\beta_0 + \frac{\beta_1(\xi-\xi_0)}{(\xi-\xi_0)^2 + (d_0/G_0)^2} \right. \\ &\quad \left. + \frac{\beta_2}{(\xi-\xi_0)^2 + (d_0/G_0)^2}\right].\end{aligned} \tag{22}$$

The terms having near singularities in Eqs. (21) and (22) can be integrated analytically as,

$$\begin{aligned}&\frac{1}{G_0^2}\int_{-1}^{1}\frac{(\xi-\xi_0)}{(\xi-\xi_0)^2 + (d_0/G_0)^2}\,\mathrm{d}\xi \\ &= \frac{1}{G_0^2}\left[\log\sqrt{(1-\xi_0)^2 + \left(\frac{d_0}{G_0}\right)^2}\right. \\ &\quad \left. - \log\sqrt{(1+\xi_0)^2 + \left(\frac{d_0}{G_0}\right)^2}\right],\end{aligned} \tag{23}$$

and

$$\begin{aligned}&\frac{1}{G_0^2}\int_{-1}^{1}\frac{\mathrm{d}\xi}{(\xi-\xi_0)^2 + (d_0/G_0)^2} \\ &= \frac{1}{G_0 d_0}\left[\tan^{-1}\left\{\frac{G_0}{d_0}(1-\xi_0)\right\} + \tan^{-1}\left\{\frac{G_0}{d_0}(1+\xi_0)\right\}\right].\end{aligned} \tag{24}$$

Also, the integral of the logarithmic function found in Eqs. (15) and (16) is given analytically by

$$\begin{aligned}&\int_{-1}^{1}\log\varepsilon\,\mathrm{d}\xi = \int_{-1}^{1}\log G_0\sqrt{(\xi-\xi_0)^2 + (d_0/G_0)^2}\,\mathrm{d}\xi \\ &= (1-\xi_0)\log\left\{G_0\sqrt{(1-\xi_0)^2 + (d_0/G_0)^2}\right\} \\ &\quad + (1+\xi_0)\log\left\{G_0\sqrt{(1+\xi_0)^2 + (d_0/G_0)^2}\right\} \\ &\quad + \frac{d_0}{G_0}\left[\tan^{-1}\left\{\frac{G_0}{d_0}(1-\xi_0)\right\} + \tan^{-1}\left\{\frac{G_0}{d_0}(1+\xi_0)\right\}\right] \\ &\quad - 2.\end{aligned} \tag{25}$$

Figure 3 compares the integrands in terms of $\partial\psi^*/\partial b$ with $\phi_2 = (1-\xi)(1+\xi)$ before and after damping out the singularity for a case where 20 eddy current nodes, i.e., only 10 boundary elements are used along the shell. The integrand behavior in Fig. 3 (a) is an example for a boundary element with $\xi_0 = 0.0$ and $d_0 = 8$ mm, while Fig. 3 (b) is for an element with $\xi_0 = 0.5$ and $d_0 = 2$ mm. The shape of the original integrand in Fig. 3 (a) is mainly the contribution of the 3rd term in the bracket of Eq. (22). In contrast, the 2nd term in the bracket is dominant to form the shape in Fig. 3 (b). In both figures the strong singularity is efficiently damped out. Notice that the modified integrand in Fig. 3 (b) still has a small edge at $\xi_0 = 0.5$. In order not to reduce the accuracy, it is recommended that the first integral on the RHS of Eq. (18) is divided into two integral intervals, $[-1, \xi_0]$ and $[\xi_0, +1]$ as long as $\xi_0 \neq \pm 1$.

2.5 Solving an ill-conditioned matrix equation – the MTSVD method

Figure 4 shows the behavior of the singular values which appeared in the singular value decomposition process for various numbers of assumed eddy current nodes, N_S. They are the results of the RELAX test problem that will be described in Sec. 3. The vertical axis represents

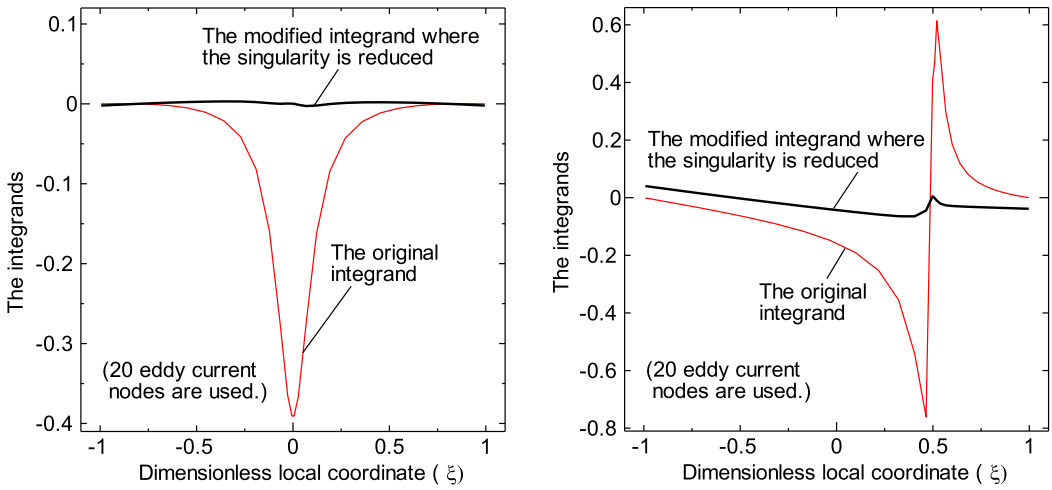

(a) $\xi_0 = 0.0,\ d_0 = 8\text{mm}$ (b) $\xi_0 = 0.5,\ d_0 = 2\text{mm}$

Fig. 3 Behaviors of integrands before and after damping out the singularity.

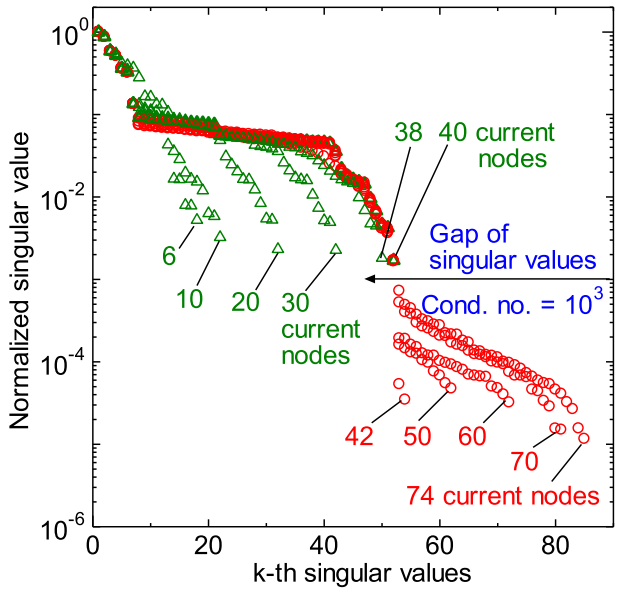

Fig. 4 Behavior of the singular values with the number of eddy current nodes (N_S).

the singular values whose maximum value is normalized to unity. The smallest singular value decreases with the increase in N_S, and it becomes less than 10^{-3} when N_S is greater than 40. A gap is commonly observed in the vicinity of 10^{-3} of the normalized singular values. It is interesting to point out that the number of singular values larger than the gap threshold is 52 ($= 2N_C + N_\psi = 2N_C + N_B$) in all cases where N_S is over 40 (see the calculation conditions described in Sec. 3.1). When the number of current nodes N_S exceeds 40, the condition number (the ratio of the largest to the smallest singular values; the reciprocal of the normalized singular value) jumps up to over 10^4.

Figures 5 (a) and 5 (b) illustrate the behaviors of some columns of the orthogonal matrix $\boldsymbol{V}$ in Eq. (14) when 60 eddy current nodes are used. These columns are often called the 'right singular vectors', which play an important role in forming the solution vector. Figure 5 (a) shows the 48th to the 52nd right singular vectors, while Fig. 5 (b) shows the 53rd to the 57th vectors. In each figure the abscissa indicates the component numbers in each vector. The 1st to the 12th components are related to the Cauchy conditions, while the numbers larger than 12 correspond to the eddy current node values.

Although there are local fine structures, as shown in Fig. 5 (a), each of the right singular vectors up to the 52nd maintains a gentle waveform as a whole. However, in Fig. 5 (b) for the vectors whose column numbers are larger than 52, the appearance changes suddenly, i.e., high frequency oscillations are observed in the eddy-current related part of each vector. Note that these right singular vectors correspond to the singular values smaller than the gap threshold found in Fig. 4. These oscillations become more marked and their magnitude increases rapidly with further increase in the column number. This means that the singular values smaller than the gap threshold cause numerical oscillations of the reconstructed eddy current density profile.

To cut out the high frequent mode, the so-called truncated singular value decomposition (TSVD) technique [15] is often used. In this technique, the regularized solution is given by

$$\boldsymbol{p}_k = \boldsymbol{V}\boldsymbol{\Lambda}_k^{-1}\boldsymbol{U}^{\mathrm{T}}\boldsymbol{g}. \tag{26}$$

Here $\boldsymbol{\Lambda}_k$ means that the singular values smaller than λ_k in $\boldsymbol{\Lambda}$ are omitted so that the condition number is not larger than a certain value. If one truncates the singular values smaller

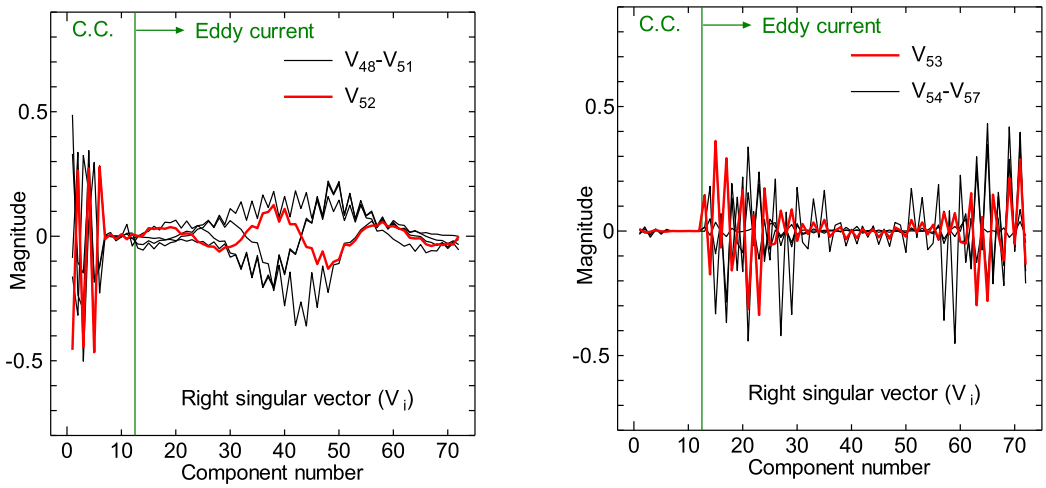

Fig. 5 Behavior of the right singular vectors.

than the gap threshold observed in Fig. 4, the improved condition numbers are around 6×10^2 in all cases.

Even with this TSVD technique, however, a numerical oscillation of $\boldsymbol{p}_k$ is observed when the smallest singular value is smaller than the gap threshold. One idea to suppress such an oscillation is to introduce a constraint, $\min \|\boldsymbol{Lp}\|$, in addition to $\min \|\boldsymbol{Dp} - \boldsymbol{g}\|$, where $\boldsymbol{L}$ means a differential operator. Elden [17] showed that the solution in this case can be written formally as

$$\boldsymbol{p}_{L,k} = (\boldsymbol{I} - (\boldsymbol{L}(\boldsymbol{I} - \boldsymbol{D}^+\boldsymbol{D}))^+\boldsymbol{L})\boldsymbol{D}^+\boldsymbol{g}, \tag{27}$$

where $\boldsymbol{I}$ is an identity matrix and $\boldsymbol{D}^+$ means a Moore-Penrose pseudoinverse [18] of the matrix $\boldsymbol{D}$. One can here use the equations

$$\boldsymbol{D}^+ = \boldsymbol{V}\boldsymbol{\Lambda}_k^{-1}\boldsymbol{U}^{\mathrm{T}}, \tag{28}$$

and

$$\boldsymbol{p}_k = \boldsymbol{D}^+\boldsymbol{g} = \boldsymbol{V}\boldsymbol{\Lambda}_k^{-1}\boldsymbol{U}^{\mathrm{T}}\boldsymbol{g}, \tag{29}$$

since Eq. (28) as a pseudoinverse of $\boldsymbol{D} = \boldsymbol{U}\boldsymbol{\Lambda}\boldsymbol{V}^{\mathrm{T}}$ satisfies all of the Penrose conditions [18]

$$\begin{aligned} &\boldsymbol{D}\boldsymbol{D}^+\boldsymbol{D} = \boldsymbol{D}, \quad \boldsymbol{D}^+\boldsymbol{D}\boldsymbol{D}^+ = \boldsymbol{D}^+, \\ &(\boldsymbol{D}\boldsymbol{D}^+)^{\mathrm{T}} = \boldsymbol{D}\boldsymbol{D}^+ \text{ and } (\boldsymbol{D}^+\boldsymbol{D})^{\mathrm{T}} = \boldsymbol{D}^+\boldsymbol{D}. \end{aligned} \tag{30}$$

Substituting Eq. (28) into Eq. (27), Hansen *et al.* [19] derived the modified TSVD (MTSVD) solution

$$\boldsymbol{p}_{L,k} = \boldsymbol{p}_k - \boldsymbol{V}_k(\boldsymbol{L}\boldsymbol{V}_k)^+\boldsymbol{L}\boldsymbol{p}_k = \boldsymbol{p}_k - \boldsymbol{V}_k\boldsymbol{z}_k, \tag{31}$$

where $\boldsymbol{V}_k = [V_{k+1}, \cdots, V_n]$ and $\boldsymbol{z}_k$ is the solution of

$$(\boldsymbol{L}\boldsymbol{V}_k)\boldsymbol{z}_k = \boldsymbol{L}\boldsymbol{p}_k. \tag{32}$$

Although there are many possible choices of $\boldsymbol{L}$, in this work one uses the following $(n-6) \times n$ matrix for a total of n unknowns:

$$\boldsymbol{L} = \begin{bmatrix} \boldsymbol{L}^{(\mathrm{N})} & \boldsymbol{0} & \boldsymbol{0} \\ \boldsymbol{0} & \boldsymbol{L}^{(\mathrm{D})} & \boldsymbol{0} \\ \boldsymbol{0} & \boldsymbol{0} & \boldsymbol{L}^{(\mathrm{E})} \end{bmatrix}. \tag{33}$$

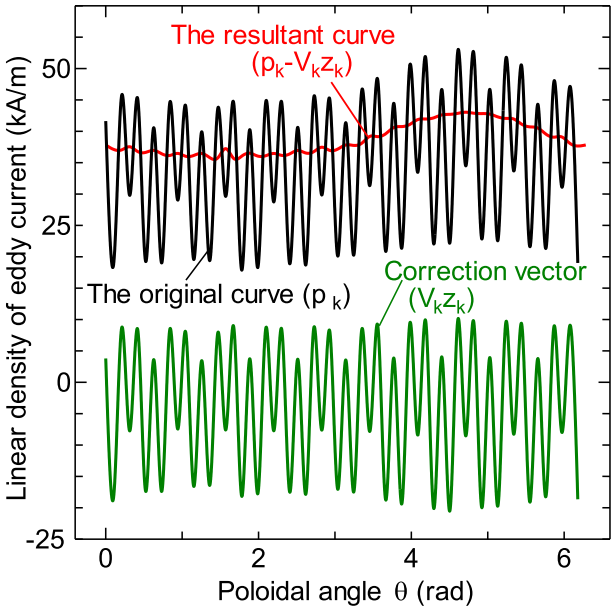

Fig. 6 Subtraction of correction vector from the original current density solution.

In Eq. (33), $\boldsymbol{L}^{(\mathrm{N})}$, $\boldsymbol{L}^{(\mathrm{D})}$ and $\boldsymbol{L}^{(\mathrm{E})}$ are discrete approximations to the second derivative operator applied to the Neumann conditions on the CCS, the Dirichlet conditions on the CCS and the current density solution on the shell surface, respectively, each of which has the tridiagonal form

$$\boldsymbol{L}^{(\mathrm{E})} = \begin{bmatrix} 1 & -2 & 1 & & & \\ & 1 & -2 & 1 & & \\ & & \ddots & \ddots & \ddots & \\ & & & 1 & -2 & 1 \end{bmatrix}, \tag{34}$$

to obtain a smooth solution.

Figure 6 illustrates the effectiveness of the MTSVD

method when applied to one of the RELAX test cases described in Sec. 3. The black curve that oscillates at high frequency is the original solution ($\boldsymbol{p}_k$) that is produced using the ordinary TSVD technique. The number of peaks in this curve, 60, agrees with the number of eddy current nodes adopted for the test case. The green curve depicts the correction vector that is given as $\boldsymbol{V}_k \boldsymbol{z}_k$ in Eq. (31). Subtracting the green curve from the black curve, i.e., following Eq. (31), one obtains the red curve where the numerical oscillation has been drastically damped out (this resultant curve is exactly the same as Fig. 8 (d) that will be shown in Sec. 3.2). Although there are slight ripples in the red corrected curve, it is worth mentioning that the number of ripples agrees not with the number of current nodes any more but with the number of sensor locations (= 40), which are the singular points, i, indicated in Eqs. (6a) and (6b).

3. Numerical Tests for the RELAX

One here considers a problem to model a limiter configuration of the RELAX device [6], as an example of a reversed field pinch device.

3.1 Problem specifications

The shell (vacuum vessel) is regarded as axisymmetric in the toroidal direction and its cross section is a circle with radius 0.25 m, which is centered at $(r, z) = (0.51\,\mathrm{m}, 0.51\,\mathrm{m})$ as shown in Fig. 7. One assumes that a 'limiter' having a length of 1 cm is located at the position $(r, z) = (0.75\,\mathrm{m}, 0.51\,\mathrm{m})$ on the inner wall of the shell. The reference distributions of magnetic flux inside the shell and the eddy current on the shell were analyzed beforehand using the RELAX-Fit code [20,21]. The signals of magnetic sensors were also known before the present inverse analyses. The reconstructed results described below are compared with the reference solutions.

The sensor locations are also illustrated in Fig. 7. One assumes 40 sensor positions around two circles with a common center at $(r, z) = (0.51\,\mathrm{m}, 0.51\,\mathrm{m})$ inside the shell: 20 points are around the circle with a radius of 0.242 m at even intervals, while the other 20 are at a distance of 0.248 m from the center. Each position is 8 mm and 2 mm away from the shell, respectively. One here hypothetically assumes that both a toroidal flux loop and a tangential probe are located at each of the 40 positions. That is, a total of 80 magnetic sensors are assumed. The tangential probe detects the magnetic field component that is tangential to the shell surface in the poloidal direction.

In the present work the CCS approximates a circle having a radius of 0.125 m and center $(r, z) = (0.51\,\mathrm{m}, 0.51\,\mathrm{m})$, as also shown in Fig. 7. The circle is divided into 3 continuous quadratic boundary elements (see Fig. 1), so that the total number of nodes is 6 (and the number of unknowns on the CCS becomes 12).

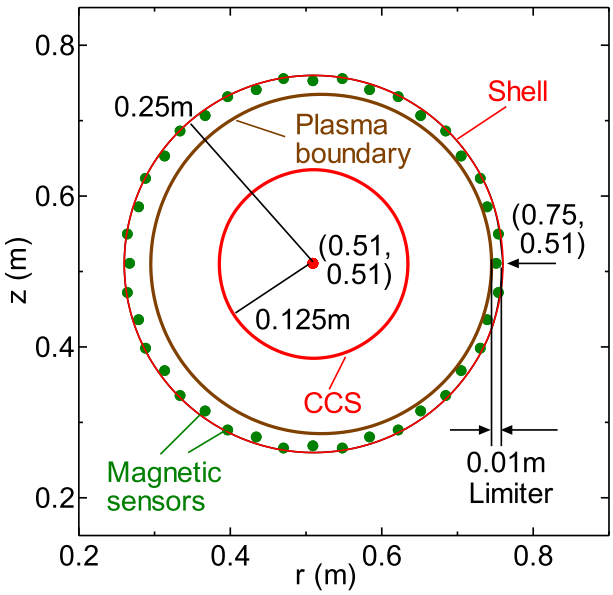

Fig. 7 Image of the RELAX limiter configuration.

3.2 Reconstruction of the eddy current density profile

The reconstructed eddy current density in units of [kA/m] was calculated so as to be continuously distributed in the poloidal direction along the shell. On the other hand, in the reference calculation 157 filament currents are assumed to be discretely and equidistantly located in the poloidal direction on the shell. For the convenience of comparison, the reference discrete current value I_{Ref} [kA] is converted to a current density value, as

$$j_{\mathrm{Ref}} = \frac{157}{2\pi R_{\mathrm{Shell}}} I_{\mathrm{Ref}} \ \ [\mathrm{kA/m}], \tag{35}$$

with the radius of the shell, R_{Shell} (= 0.25 m).

Figures 8 (a)-(d) show the variation in the eddy current density on the shell surface for the cases assuming 20, 30, 40 and 60 eddy current nodes, respectively. In each figure the vertical axis denotes the current density, while the abscissa means the poloidal angle θ that varies in the clockwise direction whose starting point ($\theta = 0$) on the shell is at the top $(r, z) = (0.51\,\mathrm{m}, 0.76\,\mathrm{m})$. The black and the red curves in Fig. 8 denote the reference and the reconstructed variation in the eddy current density, respectively.

Figure 9 shows the tendencies of the maximum and the average relative errors of the reconstructed eddy current density as a function of the number of eddy current nodes. Note here that the MTSVD technique is applied in cases where one truncates the singular values smaller than the gap threshold shown in Fig. 4, i.e., the cases where the number of current nodes (N_S) is greater than 40.

The reconstructed current profiles in Fig. 8 tend to become smoother as the number of eddy current nodes decreases. However, Fig. 9 indicates that, when the number of nodes is smaller than 14, the reconstructed profiles show

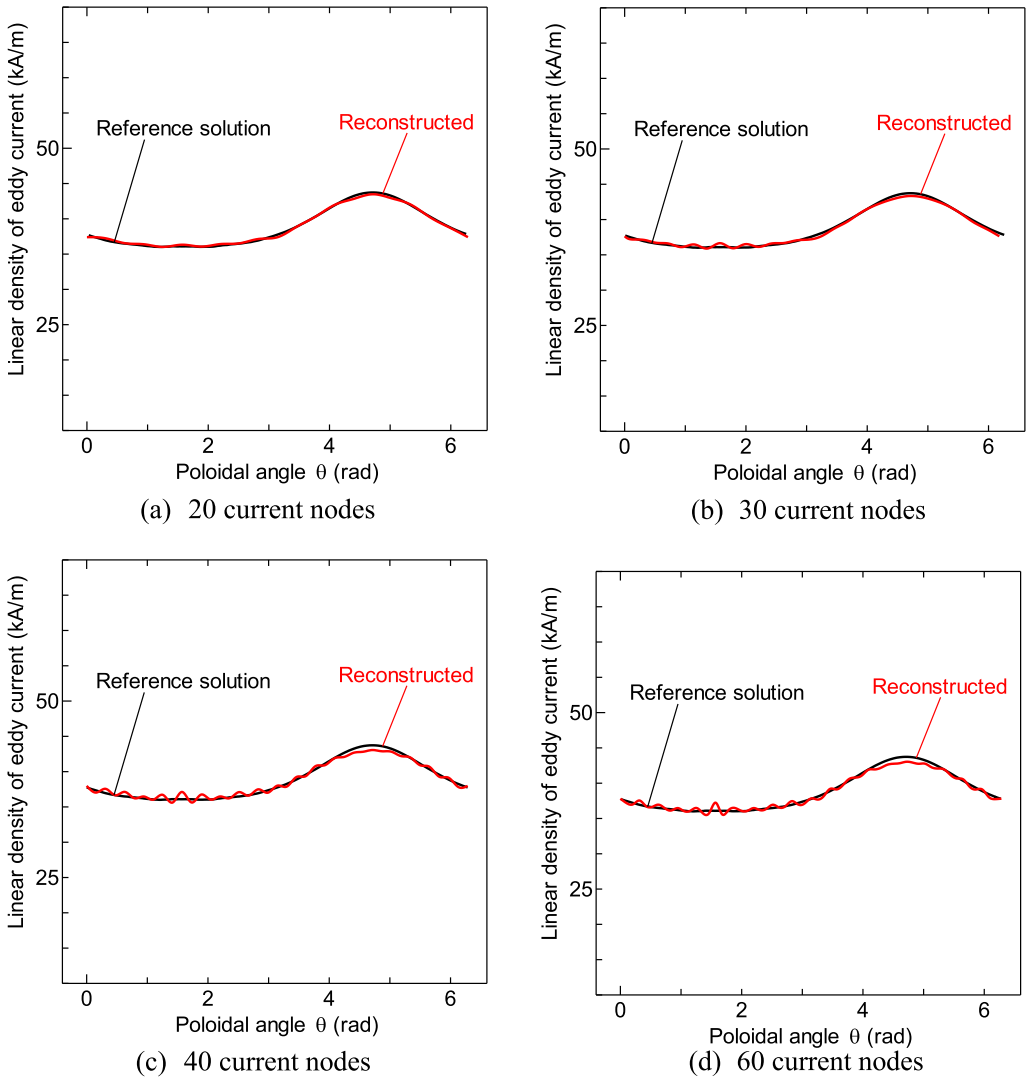

Fig. 8 Reconstruction of the eddy current profile. Figure 8 (d) is the result when using the MTSVD technique.

large errors. This is because the current profiles are extremely flattened so that they are totally different from the reference profile. In Fig. 9, the long plateau of the average error curve exists where the number of current nodes is larger than 44. The solution is still stable even for the case of 74 current nodes where the number of unknowns, 86 (= 74 current nodes + 12 conditions on the CCS) agrees exactly with the number of equations, 86 (2×40 magnetic sensors + 6 nodes on the CCS).

It is observed in Figs. 8 (c) and (d) for the cases of 40 and 60 current nodes that there are slight ripples in the reconstructed profiles. It should be pointed out that the number of ripples in Fig. 8 (d) agrees not with the number of current nodes but with the number of sensor locations (= 40), which are the singular points, i, indicated in Eqs. (6a) and (6b). As shown in Fig. 7, the sensors are located alternately at a distance of 8 mm and at the shorter distance of 2 mm from the shell. This is a possible reason for the appearance of the ripples, if the reduction in the singularity in the boundary integrals (introduced in Sec. 2.4) is still not quite sufficient. This hypothesis is supported by the results of other test calculations where all sensors are assumed to be equidistant from the shell with 60 current nodes. Figures 10 (a) and (b) show the reconstructed current density profiles assuming distances of 8 mm and 2 mm respectively. The 40 ripples found in Figs. 8 (c) and (d) are no longer conspicuous in Figs. 10 (a) and 10 (b).

3.3 Reconstruction of magnetic flux profile

The magnetic flux distributions were also reconstructed for various assumed numbers of eddy current nodes, N_S. In the following discussion, the flux distribution means that caused by only the plasma current and the eddy current on the shell; the external coil current effect (W_i^{ψ} in Eq. (6a)) is excluded in the formation of the flux distribution.

Figures 11 (a)-(d) show the reconstructed flux profiles for different numbers of current nodes. In each figure the black dashed contours show the reference solution

obtained using the RELAX-Fit code, while the red solid contours indicate the reconstructed solution.

In an ordinary CCS method analysis, the reconstructed flux solution is inaccurate in the domain where the plasma current exists. However, in the present analyses, accurate reconstructions can be observed even deep inside the plasma region. This is because the eddy current effect is dominant over the plasma current effect for the formation of the flux distribution in the RELAX device. The MTSVD method is used when the number of current nodes is greater than 40.

Figure 12 shows the tendencies of the maximum and the average relative errors of the reconstructed flux as a function of the number of eddy current nodes, N_S. The relative error is defined using values of the 'reconstructed' flux and the 'reference' flux obtained using the RELAX-Fit code, as

$$\varepsilon(\%) = 100.0 \times \left|(\text{Reconstructed} - \text{Reference})/\text{Reference}\right|, \quad (36)$$

for sampling points within the range $0.20\,\text{m} \le r \le 0.25\,\text{m}$ of a doughnut area with the center $(r, z) = (0.51\,\text{m}, 0.51\,\text{m})$, i.e., the area inside the shell but a little outside the CCS ($r = 0.125\,\text{m}$).

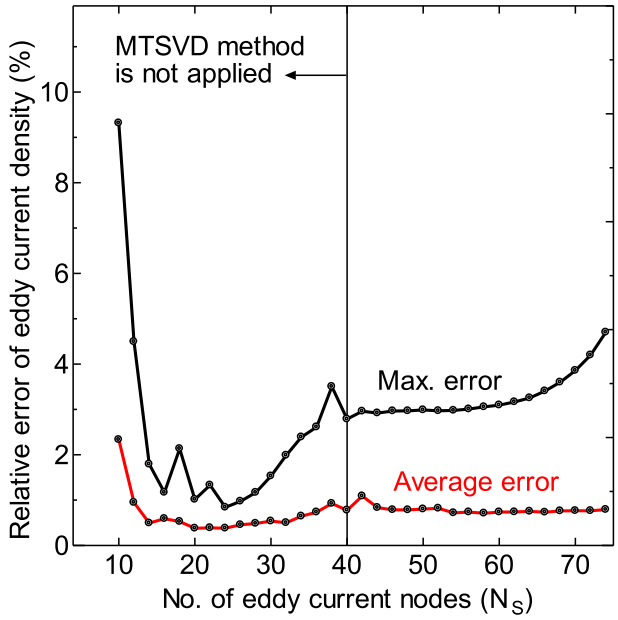

Fig. 9 Error of the reconstructed eddy current density as a function of the number of eddy current nodes (N_S).

3.4 Influence of the sensor signal noise

The effect of measurement errors on the reconstruction was also studied. Noise was numerically generated using normal (Gaussian) random numbers and added to all magnetic field and flux loop signals. The relationship between a noise-added signal $\tilde{b}_j$ and its original signal b_j is given by $\tilde{b}_j = b_j(1+\sigma \cdot G)$, where G denotes a unit Gaussian random number, while σ is the standard deviation of the Gaussian noise.

Without sensor signal noise, the reconstructed current density profile shown in Fig. 8 (a) under the adoption of 20 current nodes seems to be in good agreement with the reference profile. However, it is premature to make a conclusion that the best choice is this number of current nodes. Figure 13 shows the relative errors of reconstructed flux and eddy current density as functions of the number of current nodes under the assumption of 3% σ noise. Unfortunately the solutions are sensitive to the signal noise if the number of current nodes is less than 40.

In Fig. 13, the curve in blue indicates the variation in the condition number multiplied by 3.0%, which is the

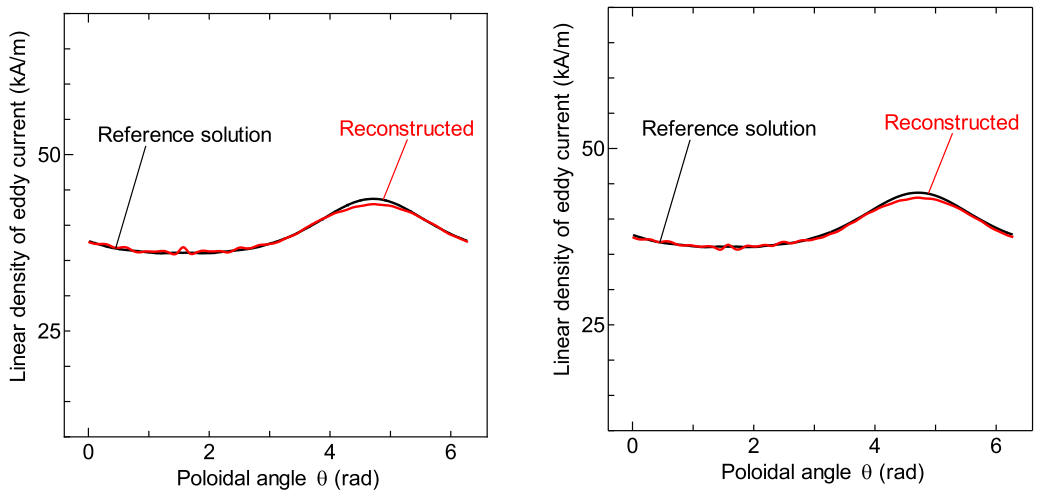

(a) Distance of 8mm (b) Distance of 2mm

Fig. 10 The eddy current profile reconstructed assuming all sensors to be equidistant from the shell.

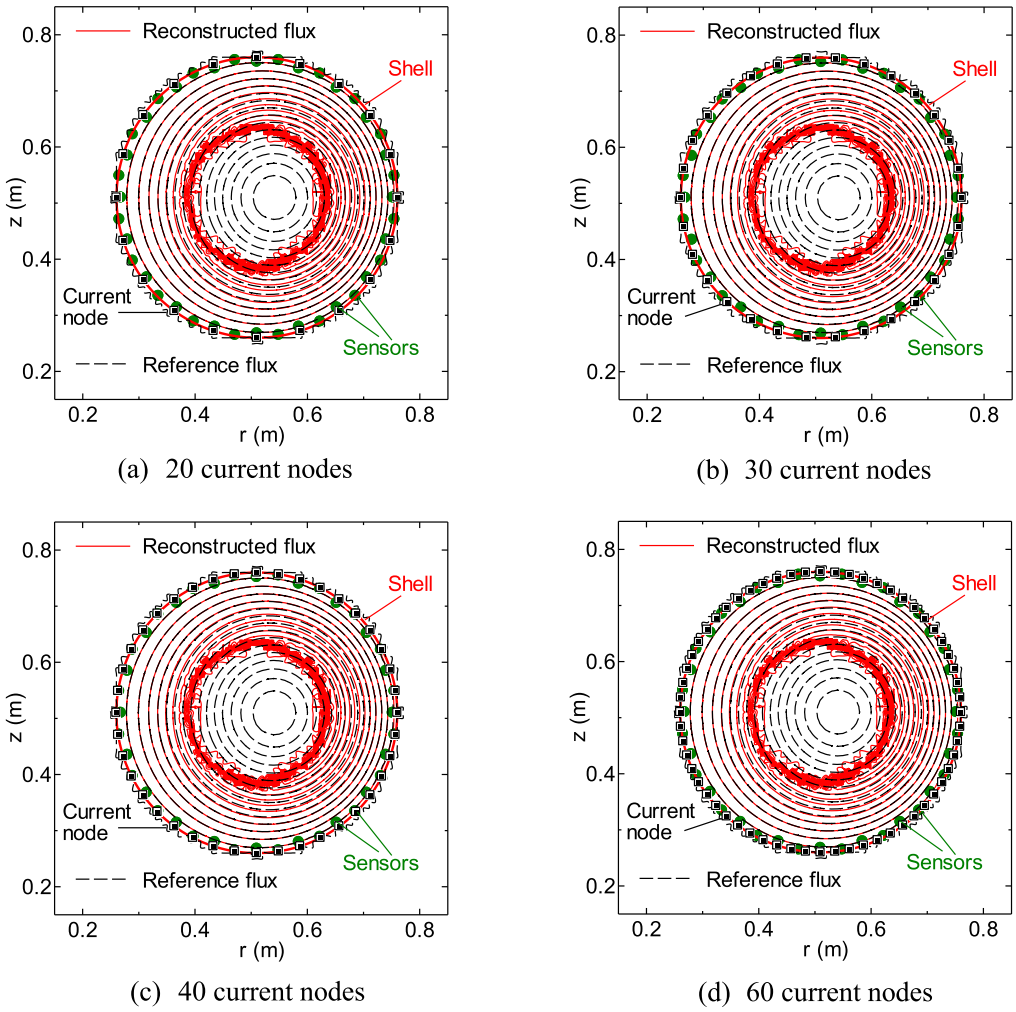

Fig. 11 Reconstruction of the magnetic flux profile. Figure 11 (d) is the result when using the MTSVD technique.

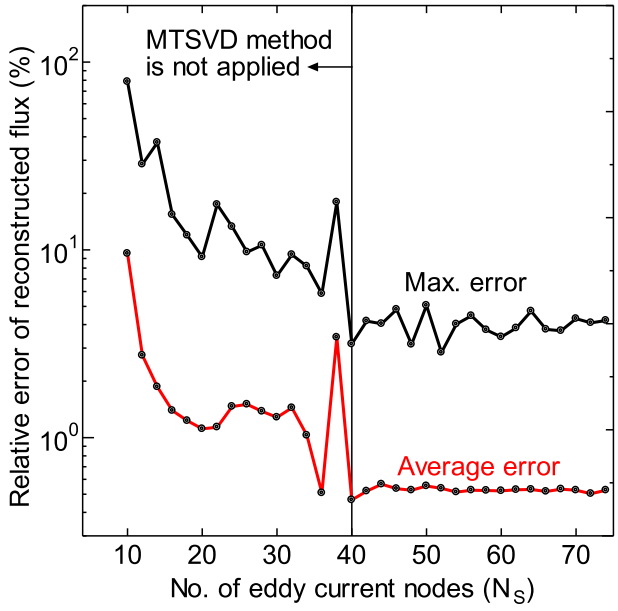

Fig. 12 Relative error of the reconstructed flux as a function of the number of eddy current nodes (N_S).

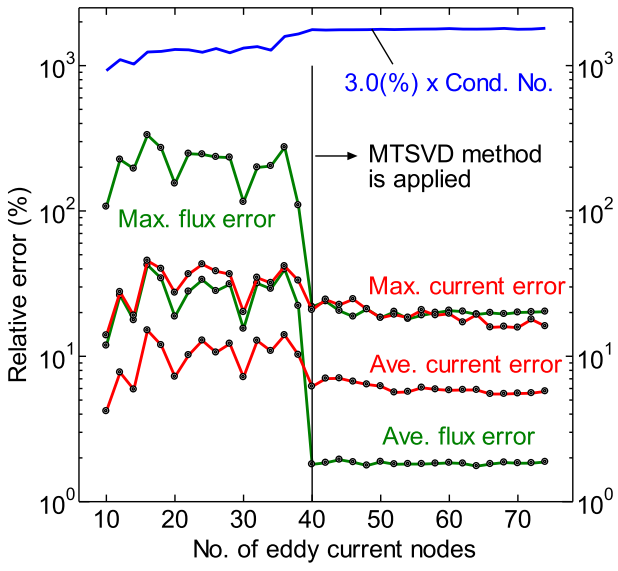

Fig. 13 Influence of the sensor signal noise when 3%σ noise is imposed.

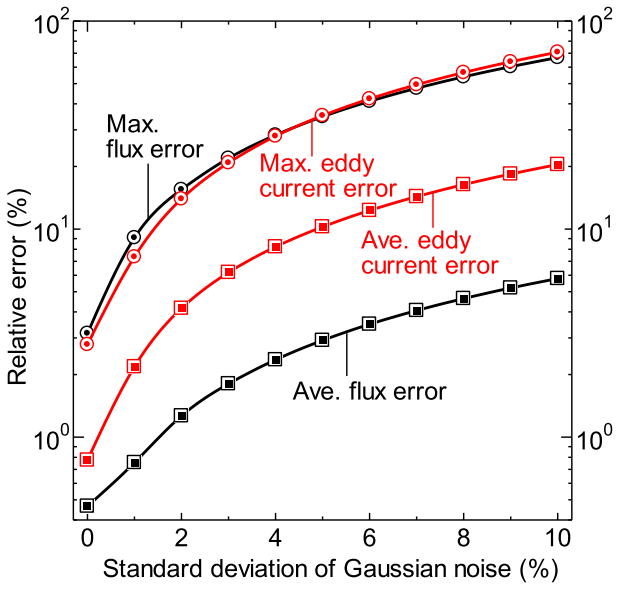

Fig. 14 Influence of the sensor signal noise when 40 eddy current nodes are assumed.

theoretical maximum of the error caused by the 3% σ noise. (The condition numbers with over 40 current nodes mean the results after truncating the small singular values.) It should be noticed that, in spite of the comparatively small condition numbers, the observed errors with fewer than 40 nodes are much larger than those with over 40 nodes. Accordingly, this phenomenon cannot be explained by the magnitude of the condition number. Rather, it is suggested that this is caused by the lack of information as a constraint in the inverse analysis. One should adopt a number of current nodes which is large enough to ensure that all singular values larger than the gap threshold, which have meaningful physical information, are taken into account in the analysis for obtaining a robust solution.

The use of 40 current nodes is an exceptional case. This case includes all singular values larger than the gap threshold, but with no need to apply the MTSVD technique because there are no singular values smaller than the gap threshold. Figure 14 indicates the variations in the maximum and the average relative errors in the flux and eddy current profiles as functions of σ for this 40 current node case. The errors increase with the increase in the noise. However, if one assumes that the signal error is no more than a few percent, it would not adversely influence the reconstructed solutions. Similar tendencies can be observed in the cases where the number of current nodes is more than 40.

4. Conclusion

The boundary integrals of the eddy current density along the shell have been added to the boundary integral equations in the conventional CCS method formulation. This new method enables one to identify accurately not only the magnetic flux profile outside the plasma but the eddy current distribution itself. Through the test calculations for the RELAX device the following conclusions have been arrived at:

(1) As the magnetic sensors are closely adjacent to the shell, the near singular boundary integrals along the shell should be accurately evaluated. This near singularity is damped out effectively with the algorithm based on the approximated distance function, as described in Sec. 2.4.
(2) To obtain a solution stable against sensor signal noise, it is important to adopt a number of eddy current nodes which is large enough to ensure that all singular values larger than the gap threshold are taken into account.
(3) If the smallest singular value is smaller than the gap threshold, a numerical oscillation of the eddy current profile is observed when using the ordinary TSVD method. However, this oscillation is eliminated effectively by applying the modified TSVD technique of Hansen *et al*.

The test calculations in Sec. 3 were made assuming 40 tangential probes and 40 flux loops. However, the same results can be expected with only 20 tangential probes and 20 flux loops, taking into account the up-down symmetry of the RELAX plasma.

The test calculations are limited to some cases in the REALX device; however, the authors believe that the techniques introduced in the present work are applicable to the problem of eddy current flow in a conductor located close to a magnetic sensor in many other devices.

Acknowledgments

This research was performed with the support and under the auspices of the NIFS Collaboration Research Program (NIFS12KLPP024 and NIFS12KNWP002). This work was also supported by the Ministry of Education, Culture, Sports, Science and Technology, Grant-in-Aid for Scientific Research (C), 24561019, 2012.

[1] K. Kurihara, Fusion Eng. Des. **51-52**, 1049 (2000).
[2] M. Itagaki, S. Yamaguchi and T. Fukunaga, Nucl. Fusion **45**, 153 (2005).
[3] M. Itagaki, T. Maeda, T. Ishimaru, G. Okubo, K. Watanabe, R. Seki and Y. Suzuki, Plasma Phys. Control. Fusion **53**(10), 105007 (2011).
[4] M. Itagaki, G. Okubo, M. Akazawa, Y. Matsumoto, K. Watanabe, R. Seki and Y. Suzuki, Plasma Phys. Control. Fusion **54**, 125003 (2012).
[5] M. Itagaki, K. Ishimaru, Y. Matsumoto, K. Watanabe, R. Seki and Y. Suzuki, Plasma Fusion Res. **8**, 1402134 (2013).
[6] S. Masamune, A. Sanpei, R. Ikezono, T. Onchi, K. Oki, T. Yamashita, H. Shimazu, H. Himura and R. Paccagnella, J. Fusion Energy **28**, 187 (2009).
[7] P. Bettini, F. Trevisan and A. Formisano, IEEE Trans. Magn. **38**(**2**), 1089 (2002).

[8] C.V. Atanasiu and L.E. Zakhanov, Phys. Plasmas **20**, 092506 (2013).
[9] V.D. Pustovitov, Plasma Phys. Control. Fusion **50**, 105001 (2008).
[10] K. Kurihara, Y. Kawamura, M. Sueoka, H. Hosoyama, I. Yonekawa, T. Suzuki, T. Oikawa, S. Ide and JT-60 Team, Fusion Eng. Des. **74**, 527 (2005).
[11] K. Nakamura, Y. Jiang, X.L. Liu, O. Mitarai, K. Kurihara, Y. Kawamata, M. Sueoka, M. Hasegawa, K. Tokunaga, H. Zushi, K. Hanada, A. Fujisawa, M. Sakamoto, H. Idei, S. Kawasaki, H. Nakashima, A. Higashijima and K. Arai, Fusion Eng. Des. **86**, 1080 (2011).
[12] C.A. Brebbia and J. Dominguez, *Boundary Elements – An Introductory Course* (Southampton, Computational Mechanics Publications, 1998).
[13] M. Itagaki and T. Fukunaga, Eng. Anal. Bound. Elem. **30**, 747 (2006).
[14] M. Itagaki and H. Shimoda, Eng. Anal. Bound. Elem. **33**, 845 (2009).
[15] P.C. Hansen, *Rank-Deficient and Discrete Ill-Posed Problems – Numerical Aspects of Linear Inversion* (Philadelphia, SIAM, 1998).
[16] H. Ma and N. Kamiya, Eng. Anal. Bound. Elem. **25**, 833 (2001).
[17] L. Eldén, BIT **22**, 487 (1982).
[18] Y. Nakamura, *Advanced Robotics: Redundancy and Optimization* (Reading, MA, Addison-Wesley, 1991).
[19] P.C. Hansen, T. Sekii and H. Shibahashi, SIAM J. Sci. Stat. Comput. **13**, 1142 (1992).
[20] A. Sanpei, K. Oki, R. Ikezoe, T. Onchi, K. Murata, H. Shimazu, T. Yamashita, S. Fujita, H. Himura, S. Masamune and J.K. Anderson, J. Phys. Soc. Jpn. **78**(**1**), 013501 (2009).
[21] J.K. Anderson, C.B. Forest, T.M. Biewer, J.S. Sarff and J.C. Wright, Nucl. Fusion **44**, 162 (2004).